

Article

Electrochemical Corrosion Behavior of Laser Welded 2205 Duplex Stainless-Steel in Artificial Seawater Environment under Different Acidity and Alkalinity Conditions

Hany S. Abdo , Asiful H. Seikh * , Ubair Abdus Samad, Ahmed Fouly  and Jabair Ali Mohammed 

Mechanical Engineering Department, King Saud University, P.O. Box 800, Al-Riyadh 11421, Saudi Arabia; habdo@ksu.edu.sa (H.S.A.); uabdussamad@ksu.edu.sa (U.A.S.); amohammed7.c@ksu.edu.sa (A.F.); jmohammed@ksu.edu.sa (J.A.M.)

* Correspondence: aseikh@ksu.edu.sa

Abstract: The electrochemical corrosion behavior of laser welded 2205 duplex stainless-steel in artificial seawater environment (3.5% NaCl solutions) with different acidity and alkalinity conditions (different pH values) was investigated using different techniques. Namely, capacitance measurements (Mott–Schottky approach), electrochemical impedance spectroscopy and potentiodynamic polarization measurements. The formation of pitting corrosion on the exposure surfaces of the tested duplex stainless-steel samples was investigated and confirmed by characterizing the surface morphology using field emission scanning electron microscope (FE-SEM). Based on the obtained results, a proportional relation has been found between pH value of the solution medium and the generated film resistance due to the processes of charge transfer, which directly affecting the pitting formation and its specifications. Since the film layer composition created on the duplex stainless-steel surface is changes depending on the pH value, it was found that different bilayer structure type was generated according to the acidity or alkalinity level. The presented bilayer is almost composed from metal oxides, such as iron oxide and chromium oxide, as confirmed by Raman Spectroscopy technique. As the pits size and its quantity increased with decreasing pH value, it can be concluded that the corrosion resistance property of the laser welded 2205 duplex stainless-steel sample is improved on the alkalinity direction of the solution. Vice versa, higher acidic solution has more ability for corrosion.



check for updates

Citation: Abdo, H.S.; Seikh, A.H.; Abdus Samad, U.; Fouly, A.; Mohammed, J.A. Electrochemical Corrosion Behavior of Laser Welded 2205 Duplex Stainless-Steel in Artificial Seawater Environment under Different Acidity and Alkalinity Conditions. *Crystals* **2021**, *11*, 1025. <https://doi.org/10.3390/cryst11091025>

Academic Editors: José L. García and Bolv Xiao

Received: 1 August 2021

Accepted: 23 August 2021

Published: 26 August 2021

Publisher's Note: MDPI stays neutral with regard to jurisdictional claims in published maps and institutional affiliations.



Copyright: © 2021 by the authors. Licensee MDPI, Basel, Switzerland. This article is an open access article distributed under the terms and conditions of the Creative Commons Attribution (CC BY) license (<https://creativecommons.org/licenses/by/4.0/>).

Keywords: 2205 duplex stainless-steel; potentiodynamic polarization; EIS; Raman spectroscopy

1. Introduction

The unique chemical composition and propitious microstructure of duplex stainless-steel (DSS) made it deservedly nominated to take the lead of the best commercial high-strength materials due to its corrosion resistance and high strength combination. The word “Duplex” in the DSS term represents the combination of ferrite and austenite when available together. DSS is composed mainly from ferrite and austenite phases with variations of percentages of each phase. Corrosion resistance and mechanical performance of DSS is depending mainly on the phase balance composition, since ferrite affects significantly the strength, toughness, and resistance to corrosion, while austenite controls the ductility with little contribution to corrosion resistance. It has been demonstrated that the most appropriate phase balance giving the optimum DSS performance is the composition of 50% ferrite and 50% austenite in sufficient Nitrogen (N₂) stream [1–3]. Welding of DSS is changing the phase composition of the base matrix, consequently, electrochemical behaviour and mechanical properties of the fusion zone (FZ) and heat-affected zone (HAZ) will definitely change according to the change in the phase balance and its proportions [4,5]. The scientific explanation behind that is the insufficient austenite reformation during cooling down, which causes a rich ferrite content in the welded spot compared to the base matrix initial

composition. That is because the formation of austenite generally occurs in the solid phase during the solidification of DSS in ferritic mode [6,7].

In some DSS grades after using the laser-welding process, and due to both rapid cooling rate and high heat input, the percentage of ferrite phase in the solidified structures is very close to 100% as reported by some researchers [8–10]. Incomplete reformation of austenite phase during the solidification step can lead to precipitation of some other phases, such as chromium nitride, which may directly affect the electrochemical behaviour represented by corrosion resistance as well as the mechanical properties of the FZ and HAZ [11,12]. 2205 duplex stainless-steel (2205-DSS) is an enhanced and developed version from DSS, which can overcome the common corrosion problems associated with the previous DSS series. 2205 DSS's main composition is 3.2–3.4% molybdenum, 4.8–6.4% nickel, 21–24% chromium, 0.12–0.19% nitrogen, and the rest is iron [13].

In order to join similar and non-similar materials by welding, a unique and high-power density welding process is used known as laser beam welding (LBW). The distinctive features of this welding technique are the reason for the popularity of this type of technique—low distortion, flexibility, rapid temperature change (heating/cooling), and deep penetration. Most importantly, heat-affected zones are narrow for this technique with very high precision. Many other types of high-quality welding techniques are already developed in order to obtain high-quality welding joints for duplex stainless-steel at extreme conditions [14,15]. The high incentives of this include the easy repeatability, weld shape control, and easy automation, combined with an extremely limited heat-influenced region. All the stated advantages are driving the interest towards the use of laser welding to be utilized as a joining technique for stainless-steels [16–18]. Regardless of the fact that laser welding is not so much recommended for duplex stainless-steel, researchers all around the globe are trying adjustments in welding parameters for this technique to be utilized because of the advantages it has to offer. In the search of alternatives from existing CO₂ and Nd:YAG lasers, fiber laser is opting to be an amazing alternative because of its high energy efficiency and exceptional beam quality. The laser technique is becoming more popular. The use of laser beams is also becoming a good option to be used in laser surface melting (LSM) and laser surface alloying (LSA) in addition to laser welding [19–23]. Furthermore, laser beams are also used in combination with other methods, such as different arc and plasma welding processes to create a hybrid in order to achieve the beneficial effect of both processes [24]. Lower maintenance, compact design, and less cooling requirements are some of the main benefits offered by industrial laser welding [25].

Duplex stainless-steel, a well-known highly corrosion-resistant material, was reported to be more corrosion-resistant at higher pH values than at lower pH in saline environments [26] though a tenacious passive film of chromium. Alkaline materials (e.g., carbonates) can combine with calcium and magnesium from the environment to form scale at high pH, which may help to protect stainless-steel from general corrosion [27]. However, it is not clear how duplex stainless-steel, with its high chromium content and passive film, will be affected at high pH exactly. Whereas, the studies conducted on the effects of chloride and pH in terms of passive behaviour for AISI 2205 duplex SS and their films are very limited.

The aim of the current work is to study the behaviour of laser welded 2205 duplex SS in saline solution with varying pH values of solution, ranging from acidity (pH-2) to alkalinity (pH-13) on AISI 2205 duplex stainless-steel. With the help of Mott–Schottky, electrochemical impedance (EIS), and potentiodynamic testing the electrochemical behaviour and passive film growth are investigated. To observe the changes in surface morphology scanning electron microscopy (SEM) was used, while the Raman spectroscopy was utilized to study the phases of oxide growth at different intervals on the surface of duplex steel.

2. Materials and Methods

The material used in the study was commercially produced 1 mm thick cold rolled 2205 duplex stainless-steel. Its chemical composition is given in Table 1.

Table 1. Chemical composition of Duplex 2205 stainless-steel in (wt%).

C	Mn	Si	S	P	B	Al
0.03	1.34	0.39	<0.003	0.03	0.0035	0.0039
Cr	Mo	Cu	Nb	Ni	Ti	Co
22.5	3.03	0.24	0.016	5.6	<0.005	0.128

Samples were cut into square centimetres (1 cm × 1 cm), then ground consecutively with different roughness SiC grit papers, starting by 500 up to 2000 grit SiC paper and, finally, polished using 0.1 µm alumina polishing powder, and after that degreased by ethanol, cleaned by distilled water, and then dried with air jet.

The laser welding process was carried out using a continuous Nd:YAG laser model PLDD-100M (ALPHALAS, Goettingen, Germany). A laser wavelength of 1070 nm, laser spot diameter of 0.8 mm and maximum mean laser power of 2000 W was used. In order to protect the molten pool from oxidation, high-purity argon gas (99.999%) was streamed at a flow rate of 15 L/min during the whole welding process period. A fixed welding speed of 30 mm/sec and laser power of 1500 W to produce high quality and full penetration butt-welded joints. All processing parameters are provided in Table 2.

Table 2. Process parameter of laser welding for joining 2205 duplex stainless-steel.

Laser Power	Welding Speed	Heat Input	Argon Flow Rate
1500 W	30 mm/s	65 J/mm	15 L/min

Both optical microscope (OM) model DM3 XL (Leica Microsystems, Bourges, France) and field emission scanning electron microscope (FE-SEM) Model: JEOL JSM-7600F (Tokyo, Japan) were used to characterized the samples surface morphology for investigating the microstructural features and analyses. In order to do that characterization, samples were cut by wire cutting from the weld's positions, then ground and polished, as in conventional metallographic procedures.

The corrosion-resistance property of this welded material was studied in three different solutions: (a) alkaline solution, (b) neutral solution, and (c) acidic solution. The 3.5% NaCl solution was taken as neutral solution with pH 7. The acidic solution with pH 2 and 5 were prepared by adding 5% HCl with 3.5% NaCl. The alkaline solution, i.e., aqueous sodium-potassium hydroxide solutions were prepared by diluting 0.1 M NaOH + 0.1 M KOH with distilled water until pH reached 10 and 13, respectively. In order to avoid carbonation effects, all prepared solutions were used immediately after preparations and becomes ready. Moreover, to accelerate the pitting process, 3.5 (wt.%) NaCl salt was added to each solution by different ratios [28,29]. The detailed solution description is given in Table 3.

Table 3. Different pH solutions used as electrolytes.

Specimen	Solution	pH
1	3.5% NaCl + 5%HCl	2
2	3.5% NaCl + 5%HCl	5
3	3.5% NaCl	7
4	3.5% NaCl + 0.1 M NaOH + 0.1 M KOH	10
5	3.5% NaCl + 0.1 M NaOH + 0.1 M KOH	13

Potentiodynamic polarization experiments of all welded samples were carried out at a scan rate of 1 mV/s using Gamry Potentiostat (Model PC/750, Louis Drive, Warminster, USA) instrument in the above-mentioned solution at room temperature. The 2205 duplex

stainless-steel samples were cleaned with acetone and ethanol after the polishing with emery papers and cloth polishers. Standard three electrode system was used to measure i_{corr} and E_{corr} of the sample. Saturated calomel electrode (SCE) was used as the reference electrode as in Figure 1.

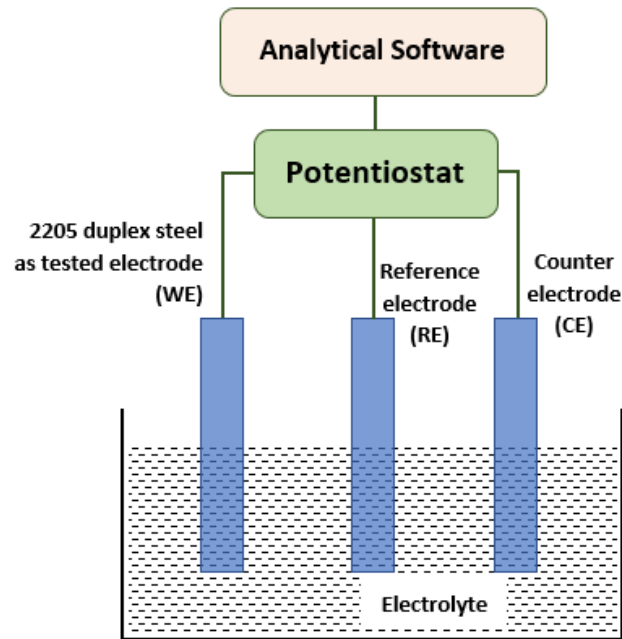


Figure 1. Schematic representation of the set-up for electrochemical studies.

Graphite was regarded as the auxiliary electrode, and the sample was the working electrode. The experiments were carried out in previously mentioned solution at room temperature. The surface area of samples exposed to the solution was differing from sample to sample. But during the time of plotting it was standardized with same sample area. The i_{corr} and E_{corr} values obtained from Figure 1 by Tafel's extrapolation method are tabulated in Table 4.

Table 4. E_{corr} and i_{corr} value of welded duplex 2205 Stainless-Steel in different pH solution.

Solution	E_{corr} (V vs. SCE)	i_{corr} (A/cm ²)
pH 13	0.3755	8×10^{-09}
pH 10	0.3518	3×10^{-08}
pH 7	0.1831	1×10^{-07}
pH 5	0.2339	6×10^{-07}
pH 2	0.3157	4×10^{-06}

For electrochemical impedance spectroscopy measurements, a three-electrode corrosion cell was used. Open circuit was done for 30 min before polarization in normal open-air environment and without solution stirring. Impedance spectroscopy experiments were carried out using 100 mV AC voltage root-mean-square and 1V DC voltage vs. at starting potential of -2 V vs. SCE. SCE in the frequency ranged from 0.01 Hz to 300 kHz at 10 cycles per decade. At each frequency, phase angles and absolute impedance were measured and both Nyquist and Bode plots were obtained. Each polarization test was repeated for three times to ensure repeatability. By using a simplex fitting model, impedance data were fitted into adequate electrical circuit (equivalent circuit). Electrochemical parameters were obtained after EIS studies from EIS curves and the EIS parameters are tabulated in Table 5.

Table 5. EIS fitting data of 2205 DSS in 3.5% NaCl solution with different pH.

Solution	Rs (ohm-cm ²)	CPE1 (ohm ⁻¹ cm ⁻² s ⁻ⁿ)	R1 (ohm-cm ²)	CPE2 (ohm ⁻¹ cm ⁻² s ⁻ⁿ)	R2 (kohm-cm ²)
pH 2	9.67	71.71	11.04	278.70	109.7
pH 5	7.94	62.81	13.12	4.43	155.90
pH 7	6.97	66.58	22.86	374.6	211.50
pH 10	5.82	78.89	33.38	239.1	267.48
pH 13	7.35	60.21	56.78	1103.3	310.60

Mott–Schottky plots were conducted for each passive film by measuring the capacitance of the passive film as a function of potential at a rate of 15 mV/step. The potential was then scanned in the anodic direction between -1.0VSCE and 1.0VSCE . An ac voltage signal of 10 mV amplitude at 1 kHz was super imposed for 2 s at each potential step, and the resultant impedance was measured and recorded as a function of potential. The 1 kHz frequency was selected for comparison with literature data.

3. Results and Discussions

3.1. Potentiodynamic Polarization Studies

As presented in Figure 2, a proportional relation is applied between pH value and corrosion rate, since the corrosion rate is increasing with increasing acidity (lower pH values). That is because the rich hydrogen ions which accelerating corrosion in low pH medium by attacking and damaging the steel upper surface layer and increasing the total weight losses. On the other hand, although the chloride ions are increasing also the corrosion rate, especially for stainless-steel in acidic solutions, but these chloride ions did not have the same corrosive effect as hydrogen ions. Wherever the protective oxide layer got destroyed on some surface portions, the chloride ions slowly penetrate to that unprotective steel surface and corrosion starts. Penetration of chlorides happens in steel according to different mechanisms, such as capillary absorption and diffusion, which leads to create pits (pitting corrosion) with irregular shape and variant depth. In alkaline solutions, mechanism is little different, since (OH^-) group is simply attracted to the steel surface, which make the passive film stable offering more protection to the steel surface [30,31]. In both neutral solution and alkaline solution corrosion resistance property is much better compared to the sample in the acidic solution.

3.2. EIS Studies

Electrochemical Impedance Spectroscopy (EIS) is a non-destructive technique used to investigate and studying the electrochemical behaviour on the metals surfaces and corrosion products forming on these surfaces. EIS spectra has been obtained for different solution pH values (2, 5, 7, 10, and 13) and plotted in Figure 3 in the form of Bode plot and Nyquist plot. Here in the Bode magnitude plot the broad low and middle frequency range exhibit a linear slope of about -1 broad (1 kHz–10 Hz) middle frequency range and constant $\log |Z|$ values vs. $\log (f)$ with a phase angle near 0° in the higher frequency region. This is the characteristic response of a capacitive behavior of surface film. Nyquist plots diagram shows a capacitive arc or semi-circle with increasing radius proportional to the increase in pH value. At the maximum value of pH (13), the overall impedance values are also maximum, which indicate a very good corrosion resistance improvement, matching the outcomes from potentiodynamic polarization curves in Figure 2.

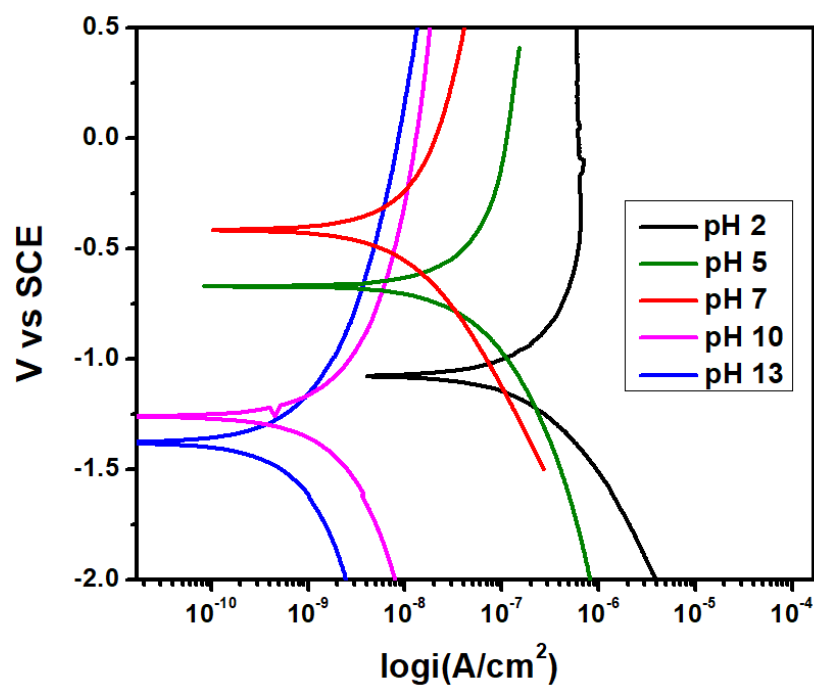


Figure 2. Potentiodynamic polarization curve of laser welded duplex 2205 stainless-steel at different pH solution.

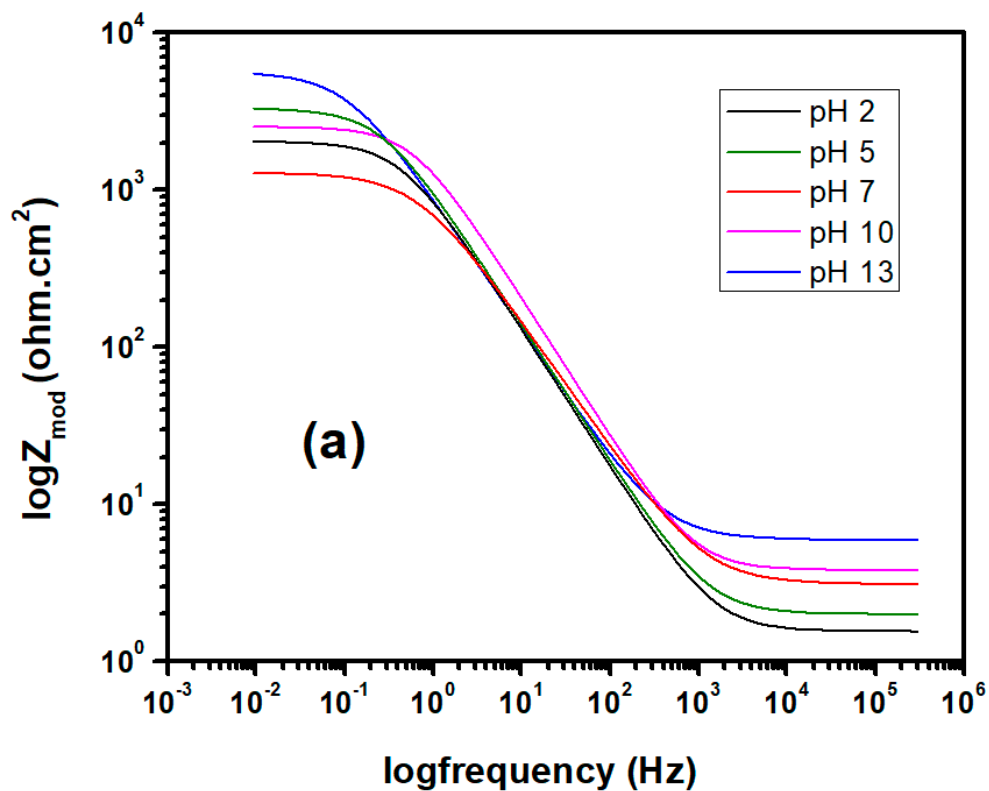


Figure 3. Cont.

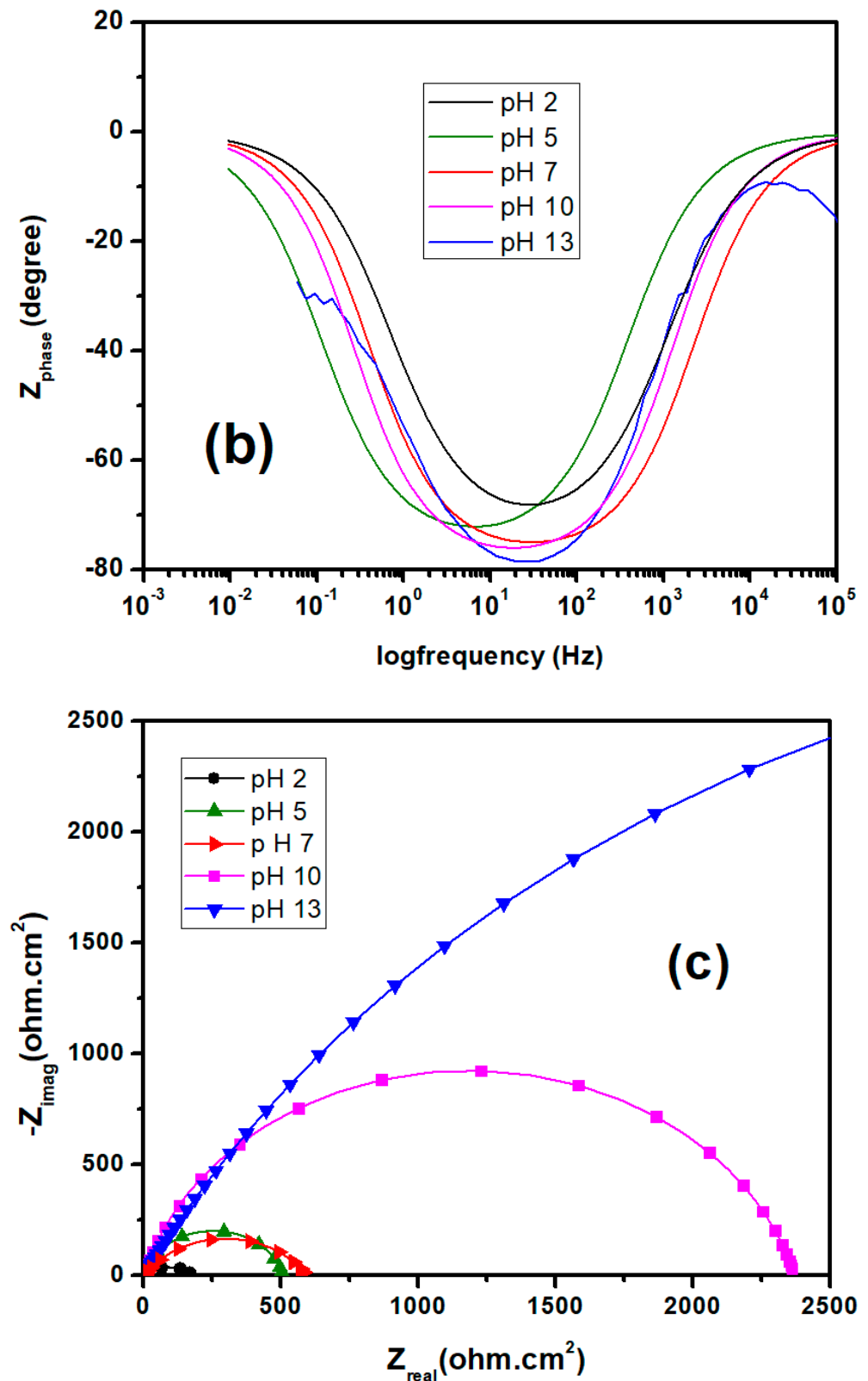


Figure 3. Bode (a) phase plot, (b) mode plot, and (c) Nyquist plot of 2205 duplex stainless-steel in different pH solution.

The kinetic parameters which could be affected by the solution acidity or alkalinity have been explored in Figure 4 represented by an appropriate equivalent electric circuit diagram [31] for the passive film generated on the surface. It could be interpreted as a

defected passive layer created the 2205 duplex stainless-steel surface during the polarization test at different pH solution. The equivalent electric circuit diagram (Figure 4) is represented by different components. CPE1 and CPE2 (constant phase element) which simulating the passive film capacitive behavior. Resistance R_1 and R_2 are corresponding to the oxide film resistance and charge-transfer resistance at solution/metal interface respectively [31,32], while R_s is the solution resistance. The fitting results of EIS for the tested 2205 duplex stainless-steel in different pH solution are listed in Table 5.

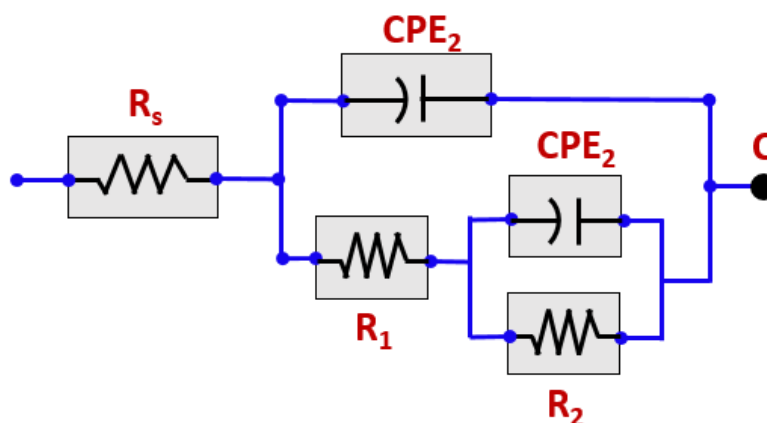


Figure 4. Equivalent circuit diagram for EIS fitting.

Based on the results presented in Table 5, the passive film resistance R_1 looks to be enhanced due to the increasing pH of the solution, indicating an enhancement of passive film generated. The total resistance ($R_1 + R_2$), which equivalent to the overall corrosion resistance of the surface, noticeably enhanced with increasing pH value of the solution.

3.3. SEM Analysis

In Figure 5 the SEM images exhibit that the samples which immersed in alkaline solution (higher pH values) has lesser pits formation. Vice versa, the samples which immersed in acidity solution (lower pH values) has larger numbers of pits with larger size as well. This explains why the corrosion rate of the samples immersed in lower pH solution is always higher.

2205 duplex stainless-steel is composed from ferrite and austenite phases as well known. Each phase has its own microstructure and corrosion resistant property, since the pitting resistance of ferrite phase is higher than that in austenite phase [32]. At the beginning, when corrosion starts to attack the steel surface, it takes place earlier in the weaker phase. In order to observe the initiation of pitting formation, FE-SEM images were taken to the surface after the potentiodynamic polarization measurements at different pH values and presented in Figure 5. Various pits with different morphologies were observed on the duplex stainless-steel surface. Number or amount of these pits and its size as well are increasing proportionally with the decrease in the pH values towards the acidity direction. It is also observed that the most of the pit is found in the base metal compared to fusion zone. It is known that the pitting corrosion preferentially attacks the austenite phase. That's why corrosion resistance is decelerating in welded joint because its lower ferrite content. Therefore, as the variation of solution pH mainly create pitting corrosion, the fusion zone and heat-affected zone (HAZ) were not much affected by corrosion attack compared to base metal.

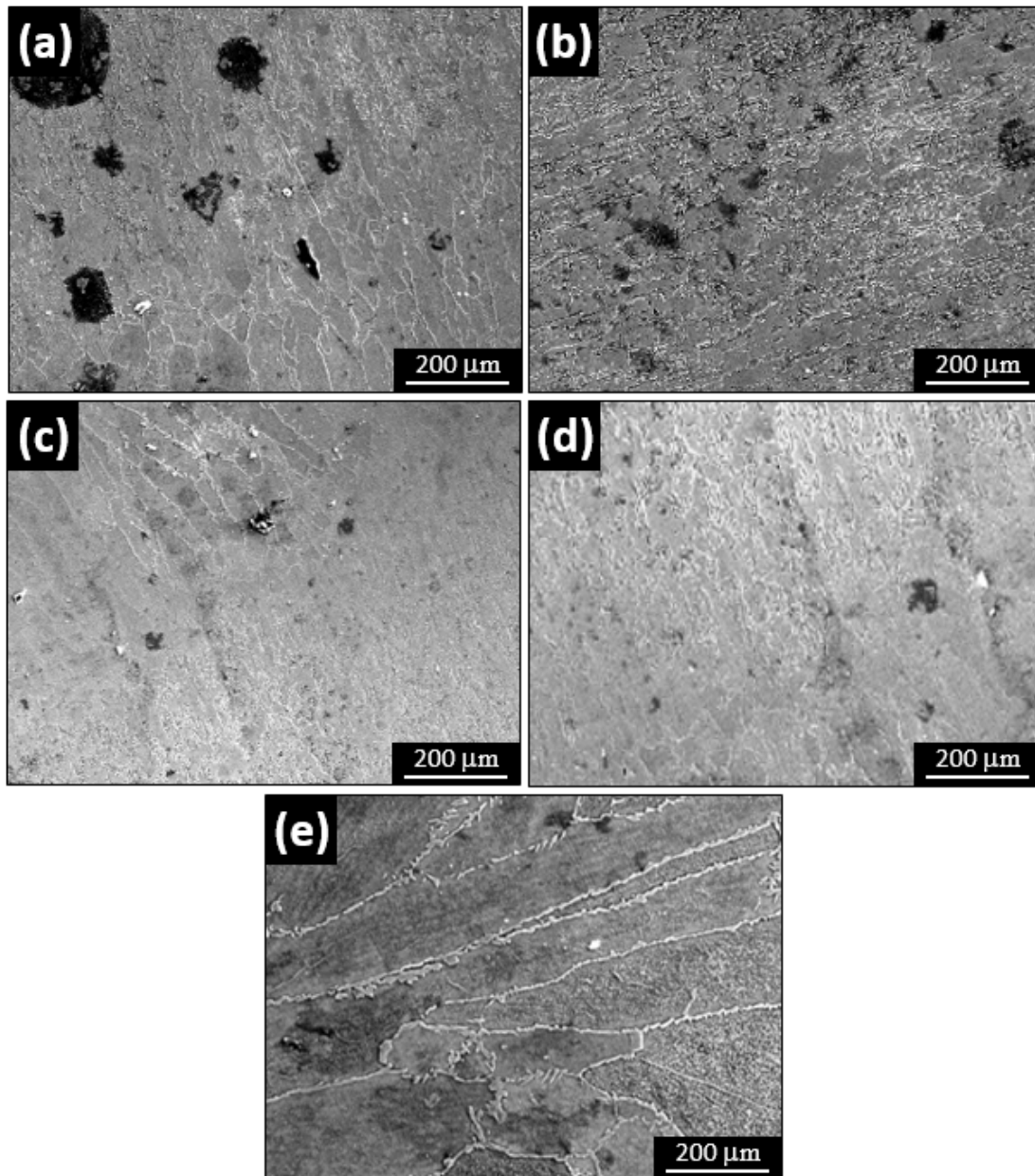


Figure 5. SEM images of 2205 duplex stainless-steel in the different solution with 3.5% NaCl at different pH (a) pH 2, (b) pH 5, (c) pH 7 (d) pH 10, and (e) pH 13.

3.4. Microstructure Analysis

Figure 6 displays the observed microstructure using optical microscopy (OM). Base matrix is recognized by the presence of austenitic grains encompassed by ferritic grains structure, which is almost higher in percentage. Austenite phase (γ) is represented by dark brown color, while the ferrite phase (δ) is represented by light brown regions.

Since the laser-welding technique always produces a very narrow heat-affected zone (HAZ), it shows approximately 10 μm in our case and barely visible as presented in Figure 5. As a result of directional crystallization due to the direction of heat flow from the welding pool towards the base matrix, characteristic dendritic structures were observed and shown in Figure 7.

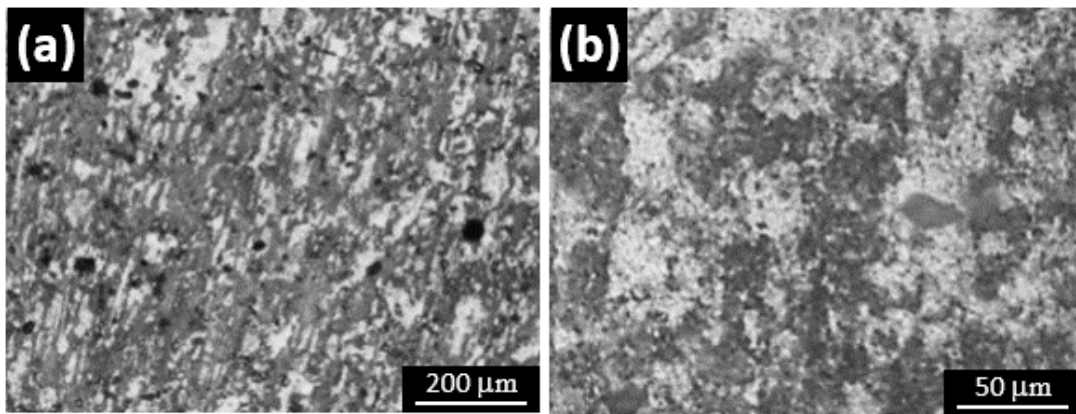


Figure 6. Microstructural features of 2205 duplex stainless-steel at different magnifications: (a) 200 μm scale bar and (b) 50 μm scale bar.

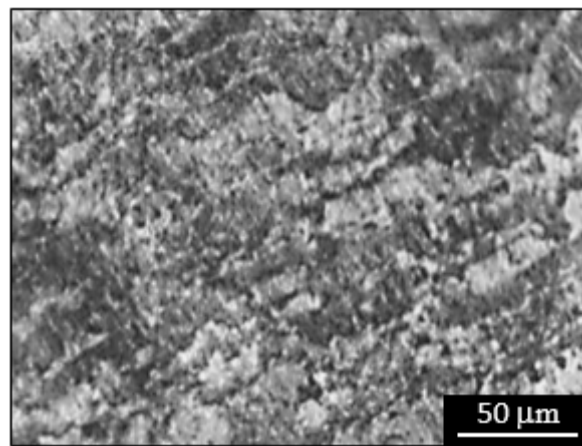


Figure 7. Microstructure images of welded joint.

Nucleation process of the austenite phase (γ) is initiated and takes place during the cooling period. Figure 8 shows the formation of the austenite grain boundary in the ferrite grains interfaces. The initial formation of the small intragranular austenite is presented in Figure 8a near to the heat-affected zone. While, in Figure 8b in fusion zone, the intragranular austenite start growing to a larger grains size. Image J software was used to measure the austenite percentage. It was found that the austenite-to-ferrite ratio in the BM sample was 51:49 while in the simulated HAZ sample the austenite content was reduced and the phase ratio was 38:62. That explains why the welded zone is better in corrosion resistance than both heat-affected zone and base metal.

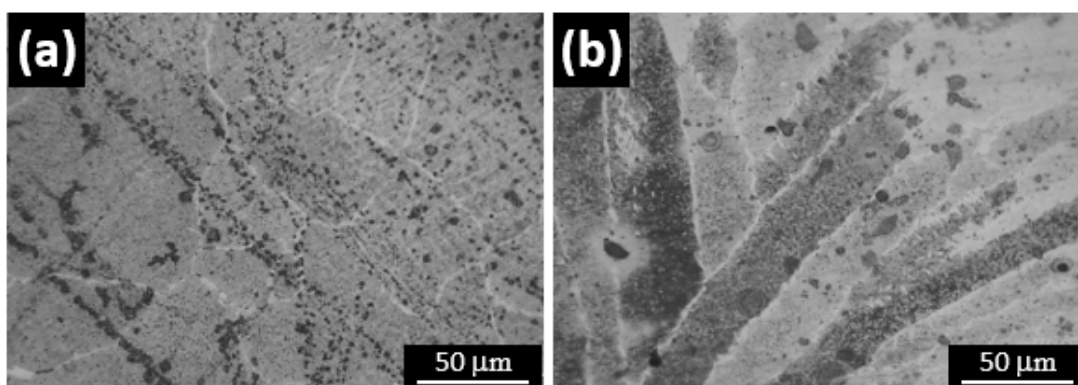


Figure 8. Microstructure of the fusion and heat-affected zones in (a) near to the heat-affected zone and (b) in the fusion zone.

3.5. Raman Measurements

Jobin Yvon (Laboratory RAM HR800) confocal micro-Raman spectrometer backscattered geometry was used to carry out the Raman measurements. Microscope objective of $10\times$ ($NA = 0.25$) was used during the analysis. The source of excitation used is Ar+ laser, which emitting at a wavelength of 514.5 nm and 1800 grooves/mm spectrometer number of grating. Before running the analysis, calibration has been done using silicon wafer at band of 520 cm^{-1} . The recorded spectra range of measurements was 200 to 2500 cm^{-1} and three reading from each sample were averaged in order to confirm the repeatability and reproducibility of collected results.

Two types from oxide scales have been formed on the 2205 duplex stainless-steel surface, which are the internal oxide scales and external oxides. The internal oxide scales known to be rich with chromium oxides $(\text{FeCr})_3\text{O}_4$ [33], while the external oxides are composed from Fe_2O_3 and Fe_3O_4 of the same phase [34]. Figure 9 shows the Raman spectra obtained by spotting the laser beam on the surface of 2205 duplex stainless-steel samples immersed in different pH solutions.

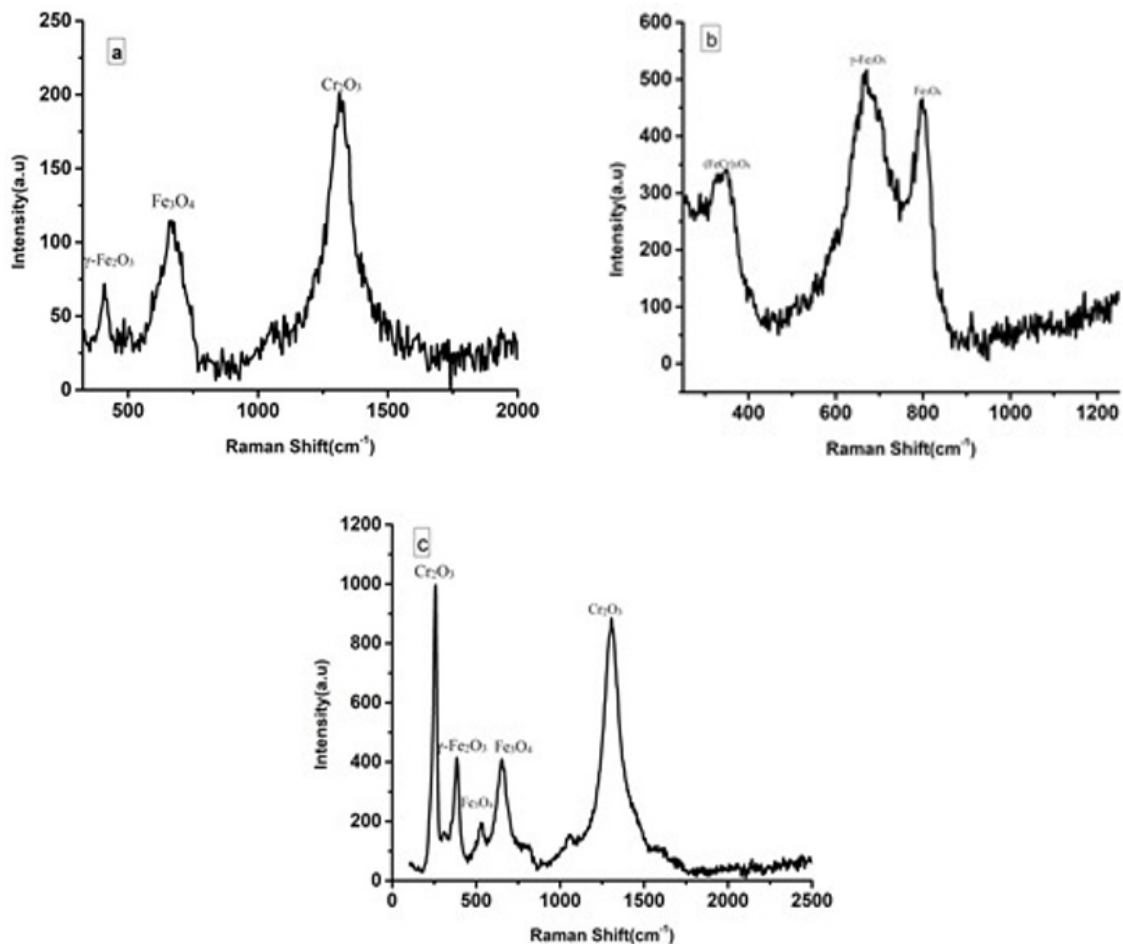


Figure 9. Raman spectroscopy images of 2205 duplex stainless-steel in the different solution with 3.5% NaCl at different pH (a) pH 2, (b) pH 7, and (c) pH 13.

Figure 9a (acidic solution with pH 2) shows the spectrum obtained where three strong peaks, located at 409 , 670 , and 1300 cm^{-1} , respectively, can be observed. According to the two last peaks the iron can be identified as a mixture of $\gamma\text{-Fe}_2\text{O}_3$ and Fe_3O_4 [34,35], whereas the peak at 1330 cm^{-1} is corresponding to the chromium oxides $(\text{FeCr})_3\text{O}_4$ [36].

In Figure 9b (neutral solution), there are three main peaks at 335 , 660 , and 790 cm^{-1} . These peaks are corresponding to the chromium oxides and iron oxides as proved in [37–39]. While in Figure 9c (alkaline solution pH 13), the two strong peaks at 560 and 680 cm^{-1}

are identified as austenite because the presence of magnetite [37], and another two medium peaks at 645 cm^{-1} and 350 cm^{-1} which can be attributed to $\gamma\text{-Fe}_2\text{O}_3$ and Cr_2O_3 , respectively [34,40].

Chromium oxide improving the corrosion-resistance property, and it is present in a higher percentage in ferrite phase than austenite. Thus, the sample in alkaline solution shows a better corrosion-resistance property.

3.6. Mott–Schottky Analysis

Figure 10 presented the Mott–Schottky plots obtained for the created passive films on 2205 duplex stainless-steel's surface after immersing in five different pH solutions. The main purpose of performing Mott–Schottky analysis is to differentiate whatever the formed passive film is simulating either p-type or n-type semiconducting characteristics [41,42]. It is clearly observed from the plot that the potential trends above 0.4 V SCE are non-linear relation, which could be attributed to the presence of two or more donor levels in the oxide film structure [43]. Moreover, from the slope of the formed passive film, it can be concluded that it is in two oxide layer structure. The inner layer is composed from chromium oxides and the outer layer is formed from iron oxides [44]. According to point defect model (PDM), oxygen vacancy and cation interstitials generated at metal–film interface, while at film–solution interface there is a cation vacancy generated [45]. These point defects can significantly affect the passive film causing its growth and breakdown once it got the ability to initiate and propagate. With the increasing of acidity, doping concentration increases for duplex stainless-steels. Yang and Luo [46] concluded that, higher doping concentration decreasing the passive film corrosion resistance. Accordingly, the worst passive film generated is always associated with the maximum value of doping concentration.

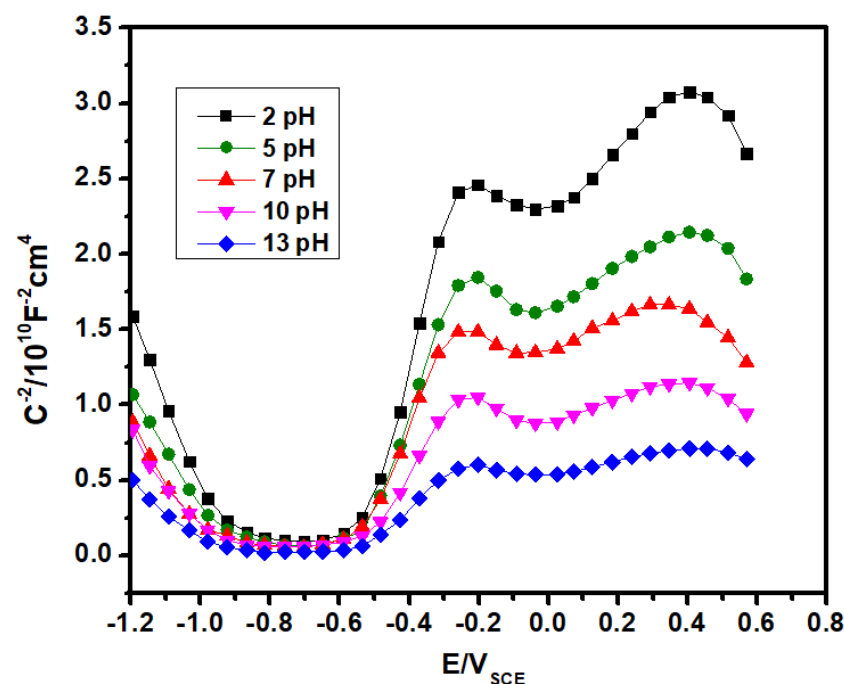


Figure 10. The Mott–Schottky plots for passive films recorded at different pH solution values for 2205 duplex stainless-steels.

4. Conclusions

1. 2205 DSS exhibited high corrosion resistance with increasing solution pH. At pH 13 it shows highest i_{corr} value compared to other samples.
2. Overall impedance values are increased with the higher pH values, which improving the corrosion resistance, and same trend was confirmed by potentiodynamic polarization curves, too.

3. FE-SEM micrographs reveals that the number and size of the pits due to pitting corrosion are increasing in the more acidic solution (low pH vales). It is also observed that the most of the pit found in the base metal compared to fusion zone. So as the variation of solution pH mainly create pitting corrosion, the fusion zone and HAZ were not much affected by corrosion attack compared to base metal.
4. Raman measurement confirms the presence of austenite and ferrite phase on the passivation layer created on the surface of 2205 duplex stainless-steel.
5. At different applied potential ranges, capacitance studies reveal that the passive films can simulate n-type and p-type semiconducting characteristics. In case of 2205 duplex stainless-steel, these passive films can be represented by two oxide layer structure. The inner layer is composed from chromium oxides and the outer layer is formed from iron oxides.

Author Contributions: Conceptualization, H.S.A.; Data curation, A.H.S.; Formal analysis, A.H.S., U.A.S., A.F. and J.A.M.; Funding acquisition, A.H.S.; Investigation, H.S.A.; Methodology, H.S.A. and U.A.S.; Project administration, H.S.A.; Resources, H.S.A.; Software, H.S.A., U.A.S., A.F. and J.A.M.; Supervision, A.H.S.; Validation, A.H.S., U.A.S. and J.A.M.; Visualization, A.H.S.; Writing—original draft, H.S.A. and A.H.S.; Writing—review & editing, H.S.A. All authors have read and agreed to the published version of the manuscript.

Funding: This research is funded by Researchers Supporting Project number (RSP-2021/373), King Saud University, Riyadh, Saudi Arabia.

Institutional Review Board Statement: Not applicable.

Informed Consent Statement: Not applicable.

Data Availability Statement: Not applicable.

Acknowledgments: The authors would like to acknowledge the Researchers Supporting Project number (RSP-2021/373), King Saud University, Riyadh, Saudi Arabia.

Conflicts of Interest: The authors declare no conflict of interest.

References

1. Shome, M. Effect of heat-input on austenite grain size in the heat-affected zone of HSLA-100 steel. *Mater. Sci. Eng. A* **2007**, *446*, 454–460. [[CrossRef](#)]
2. Abdo, H.S.; Seikh, A.H.; Mohammed, J.A.; Uzzaman, T. Ameliorative Corrosion Resistance and Microstructure Characterization of 2205 Duplex Stainless Steel by Regulating the Parameters of Pulsed Nd:YAG Laser Beam Welding. *Metals* **2021**, *11*, 1206. [[CrossRef](#)]
3. Munoz, A.I.; Anton, J.G.; Guinon, J.L.; Herranz, V.P. Inhibition effect of chromate on the passivation and pitting corrosion of a duplex stainless steel in LiBr solutions using electrochemical techniques. *Corros. Sci.* **2007**, *49*, 3200–3225. [[CrossRef](#)]
4. Chen, T.H.; Weng, K.L.; Yang, J.R. The effect of high-temperature exposure on the microstructural stability and toughness property in a 2205 duplex stainless steel. *Mater. Sci. Eng. A* **2002**, *338*, 259–270. [[CrossRef](#)]
5. Dhooge, A.; Deleu, E. Low temperature fracture toughness of thick duplex and superduplex stainless steel weldments. *Weld. World* **1997**, *39*, 47–52.
6. Kan, B.; Wu, W.; Yang, Z.; Zhang, X.; Li, J. Effects of hydrostatic pressure and pH on the corrosion behavior of 2205 duplex stainless steel. *J. Electroanal. Chem.* **2021**, *886*, 115134. [[CrossRef](#)]
7. Baeslack, W.A., III; Lippold, J.C. Phase transformation behaviour in duplex stainless steel weldments. *Met. Constr.* **1988**, *20*, 26R–31R.
8. Zeng, H.; Yang, Y.; Zeng, M.; Li, M. Effect of dissolved oxygen on electrochemical corrosion behavior of 2205 duplex stainless steel in hot concentrated seawater. *J. Mater. Sci. Technol.* **2021**, *66*, 177–185. [[CrossRef](#)]
9. Nilsson, J.O.; Karlsson, L.; Andersson, J.O. Secondary austenite formation and its relation to pitting corrosion in duplex stainless steel weld metal. *Mater. Sci. Technol.* **1995**, *11*, 276–283. [[CrossRef](#)]
10. Hertzman, S.; Huhtala, T.; Karlsoon, L.; Nilsson, J.O.; Nilsson, M.; Pettersson, R.J.; Wilson, A. Microstructure–property relations of Mo- and W-alloyed super duplex stainless weld metals. *Mater. Sci. Technol.* **1997**, *13*, 604–613. [[CrossRef](#)]
11. Hsieh, R.I.; Liou, H.Y.; Pan, Y.T. Effects of cooling time and alloying elements on the microstructure of the Gleeble-simulated heat-affected zone of 22% Cr duplex stainless steels. *J. Mater. Eng. Perform.* **2001**, *10*, 526–536. [[CrossRef](#)]
12. Liou, H.Y.; Hsieh, R.I.; Tsai, W.T. Microstructure and pitting corrosion in simulated heat-affected zones of duplex stainless steels. *Mater. Chem. Phys.* **2002**, *74*, 33–42. [[CrossRef](#)]

13. Prakash, S. Development of advanced alloys with improved resistance to corrosion and stress corrosion cracking (SCC) in power plants. In *Structural Alloys for Power Plants*; Woodhead Publishing: Cambridge, UK, 2014; pp. 294–318.
14. Łabanowski, J.; Prokop-Strzelczyńska, K.; Rogalski, G.; Fydrych, D. The effect of wet underwater welding on cold cracking susceptibility of duplex stainless steel. *Adv. Mater. Sci.* **2016**, *16*, 68–77. [[CrossRef](#)]
15. Świerczyńska, A.; Łabanowski, J.; Michalska, J.; Fydrych, D. Corrosion behavior of hydrogen charged super duplex stainless steel welded joints. *Mater. Corros.* **2017**, *68*, 1037–1045. [[CrossRef](#)]
16. Qi, K.; Li, R.; Wang, G.; Li, G.; Liu, B.; Wu, M. Microstructure and Corrosion Properties of Laser-Welded SAF 2507 Super Duplex Stainless Steel Joints. *J. Mater. Eng. Perform.* **2019**, *28*, 287–295. [[CrossRef](#)]
17. Calliari, I.; Gennari, C.; Hurtado Delgado, E.; Miranda Perez, A.F.; Rodriguez Vargas, B.R. Laser welding of plastically deformed lean duplex stainless steel. *Metall. Ital.* **2018**, *1*, 5–10.
18. Hu, S.; Zheng, D.; Zhao, G.; Li, G.; Tang, H. The effect of welded joint properties on the surface characteristics of laser-welded 2205 duplex stainless steel. *Adv. Mech. Eng.* **2018**, *10*, 1687814018797449. [[CrossRef](#)]
19. Tuz, L. Evaluation of Microstructure and Selected Mechanical Properties of Laser Beam Welded S690QL High-Strength Steel. *Adv. Mater. Sci.* **2018**, *18*, 34–42. [[CrossRef](#)]
20. Lisiecki, A.; Kurc-Lisiecka, A. Automated Laser Welding of AISI 304 Stainless Steel by Disk Laser. *Arch. Metall. Mater.* **2018**, *4*, 1663–1672.
21. Abdo, H.S.; Sarkar, A.; Gupta, M.; Sahoo, S.; Mohammed, J.A.; Ragab, S.A.; Seikh, A.H. Low-Cost High-Performance SnO₂-Cu Electrodes for Use in Direct Ethanol Fuel Cells. *Crystals* **2021**, *11*, 55. [[CrossRef](#)]
22. Tęczar, P.; Majkowska-Marzec, B.; Bartmański, M. The influence of laser alloying of Ti₁₃Nb₁₃Zr on surface topography and properties. *Adv. Mater. Sci.* **2019**, *19*, 44–56. [[CrossRef](#)]
23. Janicki, D.; Górka, J.; Kwaśny, W.; Gołombek, K.; Kondracki, M.; Żuk, M. Diode laser surface alloying of armor steel with tungsten carbide. *Arch. Metall. Mater.* **2017**, *62*, 473–481. [[CrossRef](#)]
24. Kik, T.; Górka, J. Numerical Simulations of Laser and Hybrid S700MC T-Joint Welding. *Materials* **2019**, *12*, 516. [[CrossRef](#)] [[PubMed](#)]
25. Quintino, L.; Costa, A.; Miranda, R.; Yapp, D.; Kumar, V.; Kong, C.J. Welding with high power fiber lasers—A preliminary study. *Mater. Des.* **2007**, *28*, 1231–1237. [[CrossRef](#)]
26. Abdo, H.S.; Seikh, A.H.; Mandal, B.B.; Mohammed, J.A.; Ragab, S.A.; Abdo, M.S. Microstructural Characterization and Corrosion-Resistance Behavior of Dual-Phase Steels Compared to Conventional Rebar. *Crystals* **2020**, *10*, 1068. [[CrossRef](#)]
27. Blanco, G.; Bautista, A.; Takenouti, H. Influence of the forming process of corrugated stainless steels on their corrosion behaviour in simulated pore solutions. *Cem. Concr. Compos.* **2006**, *28*, 212. [[CrossRef](#)]
28. Abdo, H.S.; Seikh, A.H.; Mohammed, J.A.; Luqman, M.; Ragab, S.A.; Almotairy, S.M. Influence of Chloride Ions on Electrochemical Corrosion Behavior of Dual-Phase Steel over Conventional Rebar in Pore Solution. *Appl. Sci.* **2020**, *10*, 4568. [[CrossRef](#)]
29. Freire, L.; Carmezima, M.J.; Ferreira, M.G.S. The passive behaviour of AISI 316 in alkaline media and the effect of pH: A combined electrochemical and analytical study. *Electrochim. Acta* **2011**, *56*, 5280. [[CrossRef](#)]
30. Abdo, H.S.; Seikh, A.H.; Fouly, A.; Hashmi, F.H. Controlling Atmospheric Corrosion of Weathering Steel Using Anodic Polarization Protection Technique. *Processes* **2021**, *9*, 1469. [[CrossRef](#)]
31. Malik, A.U.; Kutty, P.C.M.; Siddiqi, N.A.; Andijani, N.; Ahmed, S. The influence of pH and chloride concentration on the corrosion behaviour of AISI 316L steel in aqueous solutions. *Corros. Sci.* **1992**, *33*, 1809. [[CrossRef](#)]
32. Luo, H.; Dong, C.F.; Li, X.G.; Xiao, K. The electrochemical behaviour of 2205 duplex stainless steel in alkaline solutions with different pH in the presence of chloride. *Electrochim. Acta* **2012**, *64*, 211–220. [[CrossRef](#)]
33. Li, L.F.; Jiang, Z.H.; Riquier, Y. High-temperature oxidation of duplex stainless steels in air mixed gas of air and CH₄. *Corros. Sci.* **2005**, *47*, 57–68. [[CrossRef](#)]
34. Thiberau, R.J.; Brown, C.W.; Heidersbach, R.H. Raman spectra of possible corrosion products on iron at 100 to 150 °C in air. *Appl. Spectrosc.* **1978**, *32*, 532–535. [[CrossRef](#)]
35. Thierry, D.; Persson, D.; Leygraf, C.; Boucherit, N.; Hugot-Le Goff, A. Raman spectroscopy and XPS investigations of anodic corrosion films formed on Fe-Mo alloys in alkaline solutions. *Corros. Sci.* **1991**, *32*, 273–284. [[CrossRef](#)]
36. Thierry, D.; Persson, D.; Leygraf, C.; Delichere, D.; Joiret, S.; Pallota, C. In-situ Raman spectroscopy combined with X-ray photoelectron spectroscopy and nuclear microanalysis for studies of anodic corrosion film formation on Fe-Cr single crystals. *J. Electrochem. Soc.* **1988**, *135*, 305–310. [[CrossRef](#)]
37. Verble, J.R. Temperature-dependent light scattering studies of the Verwey transition and electronic disorder in magnetite. *Phys. Rev. B* **1974**, *9*, 5236–5248. [[CrossRef](#)]
38. da Cunha Belo, M.; Walls, M.; Hakiki, N.E.; Corset, J.; Picquenard, E.; Sagon, G. Composition structure and properties of the oxide films formed on the stainless steels 316 L in a primary type PWR environment. *Corros. Sci.* **1998**, *40*, 447–463. [[CrossRef](#)]
39. Beattie, I.R.; Gilson, T.R. The single-crystal Raman spectra of nearly opaque materials. *J. Chem. Soc. A* **1970**, 980–986. [[CrossRef](#)]
40. Fabis, P.; Heidersbach, R.; Brown, C.; Rockett, T. Oxide scale formation on iron chromium alloys in elevated temperature air environments. *Corrosion* **1981**, *37*, 700–711. [[CrossRef](#)]
41. Ma, H.; Cheng, X.; Li, G.; Chen, S.; Quan, Z.; Zhao, S.; Niu, L. The influence of hydrogen sulfide on corrosion of iron under different conditions. *Corros. Sci.* **2000**, *42*, 1669–1683. [[CrossRef](#)]

42. Azevedo, C.; Bezerra, P.S.A.; Esteves, F.; Joia, C.J.B.M.; Mattos, O.R. Hydrogen permeation studied by electrochemical techniques. *Electrochim. Acta* **1999**, *44*, 4431–4442. [[CrossRef](#)]
43. Gomes, W.P.; Vanmackelbergh, D. Influence of formation conditions on impedance properties of nickel passive layers formed in 1 M KOH. *Electrochim. Acta* **1996**, *41*, 967. [[CrossRef](#)]
44. Dean, M.H.; Stimming, U. The electronic properties of disordered passive films. *Corros. Sci.* **1989**, *29*, 199. [[CrossRef](#)]
45. Simoes, A.M.P.; Ferreira, M.G.S.; Rondot, B.; da Cunha Belo, M. Study of Passive Formed on AISI 304 Stainless Steel by Impedance Measurements and Photoelectrochemistry. *J. Electrochem. Soc.* **1990**, *137*, 82. [[CrossRef](#)]
46. Yang, M.Z.; Luo, J.L.; Patchet, B.M. Correlation of Hydrogen-Facilitated Pitting of AISI 304 Stainless Steel to Semiconductivity of Passive Films. *Thin Solid Film.* **1999**, *354*, 142. [[CrossRef](#)]